

Perfectly-matched-layer boundary integral equation method for wave scattering in a layered medium

Wangtao Lu ^{*} Ya Yan Lu [†] Jianliang Qian [‡]

October 13, 2016

Abstract

For scattering problems of time-harmonic waves, the boundary integral equation (BIE) methods are highly competitive, since they are formulated on lower-dimension boundaries or interfaces, and can automatically satisfy outgoing radiation conditions. For scattering problems in a layered medium, standard BIE methods based on the Green's function of the background medium must evaluate the expensive Sommefeld integrals. Alternative BIE methods based on the free-space Green's function give rise to integral equations on unbounded interfaces which are not easy to truncate, since the wave fields on these interfaces decay very slowly. We develop a BIE method based on the perfectly matched layer (PML) technique. The PMLs are widely used to suppress outgoing waves in numerical methods that directly discretize the physical space. Our PML-based BIE method uses the Green's function of the PML-transformed free space to define the boundary integral operators. The method is efficient, since the Green's function of the PML-transformed free space is easy to evaluate and the PMLs are very effective in truncating the unbounded interfaces. Numerical examples are presented to validate our method and demonstrate its accuracy.

^{*}Department of Mathematics, Michigan State University, East Lansing, MI 48824, USA. Email: wangtaol@math.msu.edu

[†]Department of Mathematics, City University of Hong Kong, Kowloon, Hong Kong. Email: mayylu@cityu.edu.hk

[‡]Department of Mathematics, Michigan State University, East Lansing, MI 48824, USA. Email: qian@math.msu.edu

1 Introduction

Scattering problems for sound, electromagnetic and elastic waves in layered media are highly relevant for practical applications [10]. Numerical methods that directly discretize the physical domain, such as the finite element method (FEM) [20], are very versatile and widely used, but they become too expensive when the scatterer is large compared with the wavelength. The boundary integral equation (BIE) methods [11] are applicable to structures with piecewise constant material parameters. These methods take care of the outgoing radiation condition automatically and reduce the dimension by one, since the integral equations are formulated on material interfaces or boundaries of obstacles. For many problems, BIE methods can outperform FEM and other domain-discretization methods, and deliver highly accurate solutions with relatively small computing efforts.

For scattering problems in a layered medium, the common BIE methods are based on the Green's function of the layered background medium [26, 28, 33], so that the integral equations are formulated on strictly local interfaces or boundaries. However, it is well known that this approach is bottlenecked by the evaluation of Sommerfeld integrals arising from the layered-medium Green's function and its derivatives. Over the past decades, many methods such as high-frequency asymptotics, rational approximations, contour deformations [7, 8, 23, 24, 25], complex images [22, 30, 31], and the steepest descent method [12, 13], have been developed to speed up the computation of Sommerfeld integrals. Unfortunately, the computational cost for evaluating the Sommerfeld integrals remains high [6].

An alternative approach is to use the free-space Green's function, but then the integral equations must also be formulated on the unbounded interfaces separating the different layers of the background medium. Various types of compactly supported functions can be used to truncate the unbounded interfaces and to suppress the artificial reflections from the edges of the truncated sections. Existing methods in this category include the approximate truncation method [18, 27], the taper function method [34, 29, 19], and the windowing function method [4, 21, 5, 14]. In particular, the windowing function method of Bruno *et al.* [5] can largely eliminate the artificial reflections, since the errors decrease superalgebraically as the window size is increased. Similar good performance can be observed in the hybrid method of Lai *et al.* [14] that combines windowed layer potentials (in physical space) with a Sommerfeld-type correction (in Fourier space) for scattering problems where the obstacles are close to or even cut through the interfaces of the background layered media.

In this paper, we develop a BIE method based on perfectly matched layers

(PMLs) for two-dimensional (2D) scattering problems in layered media. The PML technique is widely used for domain truncations in wave propagation problems [2, 3, 9, 15]. It can be regarded as a complex coordinate stretching that replaces the real independent variables in the original governing equation by complex independent variables, so that the outgoing waves are damped as they propagate into the PML region. Similar to those BIE methods based on the free-space Green's function, our BIE method avoids evaluating the expensive Sommerfeld integrals, but requires integral equations along the interfaces of the background layered medium. But instead of the free-space Green's function, we use the Green's function for the PML-transformed free space, so that the truncation of the interfaces follows automatically from the truncation of PMLs. Notice that the Green's function of the PML-transformed free space can be simply obtained by extending the argument of the usually Green's function to complex space following the definition of the complex square root function.

We implement our PML-based BIE method for 2D scattering problems involving two homogeneous media separated by a single interface. The interface is flat except in a finite section which is referred to as the local perturbation. Additional obstacles are also allowed in the homogeneous media. Two common types of incident waves are considered: a plane incident wave and a cylindrical wave due to a point source. The integral equations are established for the scattered wave satisfying Sommerfeld radiation condition at infinity. The scattered wave is defined as the difference between the total wave field and a reference wave field obtained from the same incident wave for the layered background medium (without the local perturbation of the interface and the obstacles).

BIE methods for scattering problem use many different formulations. Some of these formulations are more appropriate for large (i.e. high-frequency) problems, since they give rise to linear systems with better condition numbers, and are thus more efficient when iterative methods are used. Since our purpose is to demonstrate the effectiveness of PML-based BIEs for truncating unbounded interfaces, we adopt a simple formulation that comes from Green's representation theorem directly. In addition, we calculate the so-called Neumann-to-Dirichlet (NtD) map (mapping Neumann data to Dirichlet data on the boundary) for each subdomain with constant material parameters, so that the final linear system on interfaces or boundaries of the obstacles can be written down in a very simple form.

To approximate the integral equations, we utilize a graded mesh technique [11], a high-order quadrature rule by Alpert [1], and a newly proposed stabilizing technique. Numerical results indicate that our method is highly accurate and the truncation of the unbounded interfaces by PML is very

effective. Typically, for a PML with a thickness of one wavelength and discretized with about the same number of points as a typical segment of one wavelength, about seven significant digits can be obtained. Numerical results show that numerical error decays exponentially for S (a PML parameter representing the strength of the PML) in whatever range.

The rest of this paper is organized as follows. In sections 2 and 3, we present our PML-based BIE formulation for solving scattering problems in layered media. The numerical schemes for discretizing the integral equations are given in sections 4 and 5. Numerical examples are presented in section 6 to illustrate the performance of our method, and we conclude the paper in section 7.

2 Problem Formulation

In this paper, we mainly focus on two-dimensional TE and TM polarized scattering problems in a planar layered medium with local perturbations and/or obstacles. To clarify our methodology in a simpler setting, we assume that only local perturbations exist in the medium in the following. In general, obstacles make no noticeable difficulties for the scattering problem.

As illustrated in Figure 1, the layered medium is x_3 -invariant and consists

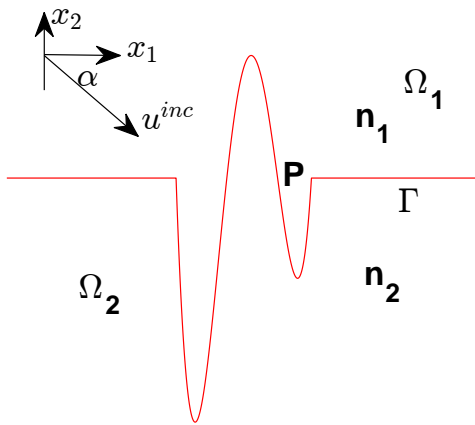


Figure 1: Profile of a 2D layered medium.

of two homogeneous layers Ω_j with constant refractive index n_j for $j = 1, 2$. The interface Γ separating the two layers is flat on $x_2 = 0$ but contains a

local perturbation curve P , smooth or piecewise smooth. Here, (x_1, x_2, x_3) denotes the standard Cartesian coordinate system.

The total field u^{tot} , representing the x_3 -component of electric field in TE polarization or the x_3 -component of magnetic field in TM polarization, solves

$$\Delta u^{tot} + k_0^2 n_j^2 u^{tot} = 0, \quad \text{in } \Omega_j, \quad (1)$$

$$[u^{tot}] = 0, \quad \left[\frac{\eta_j \partial u^{tot}}{\partial \boldsymbol{\nu}} \right] = 0, \quad \text{on } \Gamma, \quad (2)$$

where $k_0 = \frac{2\pi}{\lambda}$ is the freespace wavenumber, λ is the wavelength, $\boldsymbol{\nu}$ denotes the unit normal vector along Γ pointing toward Ω_2 , $[f]$ denotes the jump of the quantity f across Γ , $\eta_j = 1$ in TE polarization and $\eta_j = \frac{1}{n_j^2}$ in TM polarization. Let u^{inc} be an incident wave from the upper medium Ω_1 , and then one usually rewrites

$$u^{tot} = \begin{cases} u^{inc} + u_1^r, & \text{in } \Omega_1, \\ u_2^t, & \text{in } \Omega_2, \end{cases} \quad (3)$$

where u_1^r represents the reflective wave in Ω_1 and u_2^t represents the transmitted wave in Ω_2 .

In the following, we focus on two common types of incident waves, a plane incident wave and a cylindrical wave due to a source $x^* = (x_1^*, x_2^*) \in \Omega_1$. In the latter case, equation (1) should be replaced by

$$\Delta u^{tot} + k_0^2 n_j^2 u^{tot} = -\delta(x, x^*), \quad \text{in } \Omega_j, \quad (4)$$

so that the total field u^{tot} represents a layered-medium Green's function at the source x^* .

We first discuss the case for plane incident waves. Suppose the incident wave is given by $u^{inc} = e^{ik_0 n_1 (x_1 \cos \alpha - x_2 \sin \alpha)}$, where $\alpha \in [0, \pi]$ denotes the angle between the wave direction and the positive x_1 -axis. Neither u_1^r nor u_2^t satisfies the Sommerfeld radiation condition since neither of them is outgoing in all directions. To extract an outgoing wave field, we need a reference solution, denoted by u_0^{tot} , to the scattering problem with perfectly flat interface $x_2 = 0$ and with the same incident wave u^{inc} . One easily gets that

$$u_0^{tot} = \begin{cases} e^{ik_0 n_1 (x_1 \cos \alpha - x_2 \sin \alpha)} + (T - 1)e^{ik_0 n_1 (x_1 \cos \alpha + x_2 \sin \alpha)}, & \text{in } \Omega_1, \\ T e^{ik_0 n_1 x_1 \cos \alpha - ik^* x_2}, & \text{in } \Omega_2, \end{cases} \quad (5)$$

where

$$k^* = k_0 \sqrt{n_2^2 - n_1^2 \cos^2 \alpha},$$

$$T = \frac{2}{1 + \frac{k^* \eta}{k_0 n_1 \sin \alpha}},$$

and $\eta = \eta_1/\eta_2$. Then,

$$u^s = u^{tot} - u_0^{tot} := \begin{cases} u_1^s & \text{in } \Omega_1, \\ u_2^s & \text{in } \Omega_2, \end{cases} \quad (6)$$

defines an outgoing wave that satisfies

$$\Delta u_j^s + k_0^2 n_j^2 u_j^s = 0, \quad \text{in } \Omega_j, \quad (7)$$

$$\lim_{r \rightarrow \infty} r^{-1/2} \left(\frac{\partial u_j^s}{\partial r} - i k_0 n_j u_j^s \right) = 0, \quad \text{in } \Omega_j. \quad (8)$$

The transmission condition (2) then becomes

$$u_1^s|_{\Gamma} - u_2^s|_{\Gamma} = -[u_0^{tot}], \quad (9)$$

$$\eta_1 \frac{\partial u_1^s}{\partial \nu} \Big|_{\Gamma} - \eta_2 \frac{\partial u_2^s}{\partial \nu} \Big|_{\Gamma} = - \left[\eta_j \frac{\partial u_0^{tot}}{\partial \nu} \right]. \quad (10)$$

We note that away from the local perturbation curve P , $u^s = u_1^s = u_2^s$ and $\eta_1 \partial_{\nu} u_1^s = \eta_2 \partial_{\nu} u_2^s$ on Γ .

On the other hand, if the incident wave is a cylindrical wave $u^{inc} = \frac{i}{4} H_0^{(1)}(k_0 n_1 |x - x^*|)$ due to a source point $x^* \in \Omega_1$. In this case, one easily obtains that, by defining

$$u_0^{tot} = \begin{cases} u^{inc}, & \text{in } \Omega_1, \\ 0, & \text{in } \Omega_2, \end{cases} \quad (11)$$

the difference wave field $u^s = u^{tot} - u_0^{tot}$ defines an outgoing wave.

In a typical BIE formulation, the computation of u^s in the whole plane can be reduced to computing u_j^s and $\partial_{\nu} u_j^s$ on Γ , governed by the transmission conditions (9) and (10). To solve (9) and (10), we require a relation between u_j^s and $\partial_{\nu} u_j^s$ for $j = 1, 2$. In this paper, we make use of Neumann-to-Dirichlet maps \mathcal{N}_j that satisfies $u_j^s = \mathcal{N}_j \partial_{\nu} u_j^s$ on the boundary Γ for each outgoing wave $u_j^s, j = 1, 2$. Then, (9) and (10) become

$$\begin{bmatrix} \mathcal{N}_s^1 & -\mathcal{N}_s^2 \\ \eta_1 \mathcal{I} & -\eta_2 \mathcal{I} \end{bmatrix} \begin{bmatrix} \partial_{\nu} u_1^s|_{\Gamma} \\ \partial_{\nu} u_2^s|_{\Gamma} \end{bmatrix} = \begin{bmatrix} -[u_0^{tot}] \\ -[\eta_j \partial_{\nu} u_0^{tot}] \end{bmatrix}, \quad (12)$$

where \mathcal{I} denotes the identity operator. On solving (12), we immediately obtain that $u_j^s|_{\Gamma} = \mathcal{N}_s^j \partial_{\nu} u_j^s|_{\Gamma}$.

In practice, since Γ is unbounded and since u_j^s decays slowly at infinity, it is impossible to find a finite-dimensional matrix to accurately approximate \mathcal{N}_s^j by directly discretizing the whole boundary of Γ without truncating it. To resolve this issue, we use a PML to enclose the local perturbation curve P so that any outgoing wave can be absorbed. Therefore, local transmission condition can be imposed on a finite section of Γ including S . In doing so, we first need to construct NtD maps for domains in a PML environment, and this relies on boundary integral equations.

3 Boundary integral equation in a half space

Without loss of generality, we consider the outgoing solution u_1^s in Ω_1 , that satisfies

$$\Delta u_1^s + k_0^2 n_1^2 u_1^s = 0, \quad (13)$$

$$\lim_{r \rightarrow \infty} r^{1/2} \left(\frac{\partial u_1^s}{\partial r} - ik_0 n_1 u_1^s \right) = 0, \quad r = |x|, \quad (14)$$

for $x \in \Omega_1$. To simplify the presentation in this section, we assume that the piecewise smooth curve S is bounded by a box $[-a_1, a_1] \times [-a_2, a_2]$ for $a_j > 0$. Unless otherwise specified, we will suppress the subscript 1 indexing the domain Ω_1 so that we use Ω , u^s , and n to denote Ω_1 , u_1^s , and n_1 , respectively.

3.1 BIE in physical domain

As is well-known, the fundamental solution to equation (13) is

$$G(x, y) = \frac{i}{4} H_0^{(1)}(k_0 n |x - y|), \quad (15)$$

which solves

$$\Delta_x G(x, y) + k_0^2 n^2 G(x, y) = -\delta(x - y), \quad (16)$$

for $x, y \in \Omega$.

As shown in Figure 2, to truncate the unbounded interface Γ , we place a box bounded by $\Gamma^+ \cup \Gamma^-$ to enclose the local perturbation curve P so that Γ truncated by the box becomes a bounded curve Γ_{AB} , which is composed of AP_L , P , and $P_R B$. Clearly, Ω is truncated into a domain Ω^s bounded by $\Gamma^s = \Gamma_{AB} \cup \Gamma^+$, where Γ^+ is the dashed line above Γ_{AB} .

According to [11], one easily obtains the following representation theorem

$$u^s(x) = \int_{\Gamma^s} \partial_\nu G(x, y) u^s(y) - G(x, y) \partial_\nu u^s(y) ds(y), \quad (17)$$

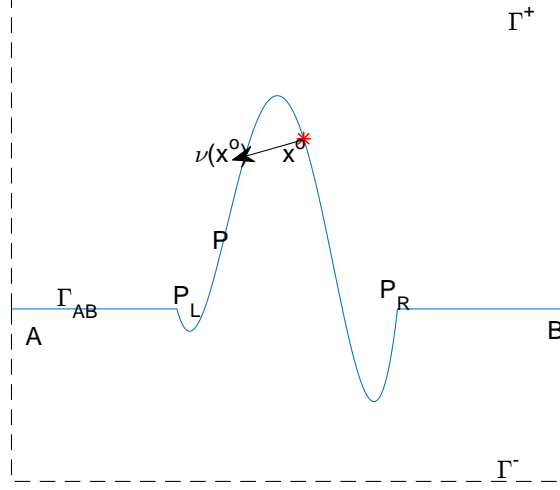


Figure 2: Profile of a 2D layered medium with direct truncation.

for $x \in \Omega^s$. As x approaches Γ^s , one gets the following boundary integral equation (see [11, 16])

$$(\mathcal{K} - \mathcal{K}_0[1])[u^s](x) = \mathcal{S}[\partial_\nu u^s](x), \quad (18)$$

for $x \in \Gamma^s$. Here, we have defined the following boundary integral operators

$$\mathcal{S}[\phi](x) = 2 \int_{\Gamma^s} G(x, y) \phi(y) ds(y), \quad (19)$$

$$\mathcal{K}[\phi](x) = 2 \int_{\Gamma^s} \partial_\nu G(x, y) \phi(y) ds(y), \quad (20)$$

$$\mathcal{K}_0[\phi](x) = 2 \int_{\Gamma^s} \partial_\nu G_0(x, y) \phi(y) ds(y), \quad (21)$$

where $G_0(x, y) = \frac{1}{2\pi} \log|x - y|$ is the Green's function of Laplacian equation $\Delta u = 0$, and \int denotes the Cauchy principal integral. Therefore, one obtains the NtD operator $\mathcal{N} = (\mathcal{K} - \mathcal{K}_0[1])^{-1} \mathcal{S}$ that maps $\partial_\nu u^s$ to u^s on the bounded curve Γ^s .

Now, a significant question arises: what boundary conditions should we impose on Γ^+ ? One may directly specify that $u^s \approx 0$ and $\partial_\nu u^s \approx 0$ on Γ^+ to truncate the NtD operator \mathcal{N} onto Γ_{AB} . Unfortunately, the outgoing wave $u^s(x)$ can decay slowly as x approaches infinity in Ω . Of course, we may place Γ^+ sufficiently far away from the perturbation curve P . However, the

computational domain can become extremely large whereas the boundary condition still maintains a low-order accuracy. To address this issue, we propose to introduce a PML to surround the local perturbation P , as will be presented below.

3.2 Green's representation theorem in PML-transformed domain

Specifically, we introduce the complex coordinate stretching function $\tilde{x}(x) = (\tilde{x}_1(x_1), \tilde{x}_2(x_2))$ by defining

$$\tilde{x}_l(x_l) = x_l + i \int_0^{x_l} \sigma_l(t) dt, \quad (22)$$

for $l = 1, 2$, where we take

$$\sigma_l(t) = \sigma_l(-t), \sigma_l = 0 \text{ for } |t| \leq a_l, \text{ and } \sigma_l(t) \geq 0 \text{ for } |t| \geq a_l. \quad (23)$$

Domains with nonzero σ_l are called the *perfectly matched layer*. Since σ_l is 0 in $[-a_1, a_1] \times [-a_2, a_2]$, the PML does not overlap the local perturbation P ; the setup of $\sigma_l(t)$ will be discussed later.

Based on (17), we can analytically continue u^s onto the domain $\tilde{\Omega}^s = \{\tilde{x}(x) | x \in \Omega^s\}$ by defining

$$u^s(\tilde{x}) = \int_{\Gamma^s} \partial_\nu G(\tilde{x}, y) u^s(y) - G(\tilde{x}, y) \partial_\nu u^s(y) dy. \quad (24)$$

According to [9], one sees that $u^s(\tilde{x})$ satisfies

$$\tilde{\Delta} u^s(\tilde{x}) + k_0^2 n^2 u^s(\tilde{x}) = 0, \quad \text{in } \tilde{\Omega}^s, \quad (25)$$

where $\tilde{\Delta} = \partial_{\tilde{x}_1}^2 + \partial_{\tilde{x}_2}^2$. Defining the complexified function $\tilde{u}^s(x) = u^s(\tilde{x})$ on Ω^s , we see that equation (25) can be rewritten by the chain rule as

$$\nabla \cdot (\mathbf{A} \nabla \tilde{u}) + k_0^2 n^2 J \tilde{u} = 0, \quad (26)$$

where $\alpha_1(x_1) = 1 + i\sigma_1(x_1)$, $\alpha_2(x_2) = 1 + i\sigma_2(x_2)$, $\mathbf{A} = \text{diag}\{\alpha_2/\alpha_1, \alpha_1/\alpha_2\}$, and $J(x) = \alpha_1(x_1)\alpha_2(x_2)$.

As shown in [15], the fundamental solution to (26) is

$$\tilde{G}(x, y) = G(\tilde{x}, \tilde{y}) = \frac{i}{4} H_0^{(1)}(k_0 n \rho(\tilde{x}, \tilde{y})), \quad (27)$$

where the complexified distance function ρ is defined to be

$$\rho(\tilde{x}, \tilde{y}) = [(\tilde{x}_1 - \tilde{y}_1)^2 + (\tilde{x}_2 - \tilde{y}_2)^2]^{1/2}, \quad (28)$$

Similarly, in the limit case when $k_0 \rightarrow 0^+$, one obtains the representation formula

$$\tilde{u}_0(x) = \int_{\tilde{\Gamma}} \{\partial_{\nu_c} \tilde{G}_0(x, y) \tilde{u}_0(y) - \tilde{G}_0(x, y) \partial_{\nu_c} \tilde{u}_0(y)\} ds(y), \quad (31)$$

for the complexified Laplacian equation

$$\tilde{\Delta} u_0(\tilde{x}) = \nabla \cdot (\mathbf{A} \nabla \tilde{u}_0(x)) = 0, \quad x \in \Omega^s. \quad (32)$$

Correspondingly, the related fundamental solution becomes,

$$\tilde{G}_0(x, y) = -\frac{1}{2\pi} \log \rho(\tilde{x}, \tilde{y}). \quad (33)$$

3.3 PML-NtD operator

Based on the two representation formulae (30) and (31), we are ready to develop the Neumann-to-Dirichlet (NtD) operator on Γ^s .

Since $\tilde{u}_0 = 1$ solves (32), we get from (31) that

$$1 = \int_{\Gamma^s} \partial_{\nu_c} \tilde{G}_0(x, y) ds(y), \quad (34)$$

when $x \in \Omega^s$. Now, (30)– $\tilde{u}^s(x) \times$ (34) yields

$$0 = \int_{\Gamma^s} \{(\partial_{\nu_c} \tilde{G}(x, y) \tilde{u}^s(y) - \partial_{\nu_c} \tilde{G}_0(x, y) \tilde{u}^s(x)) - \tilde{G}(x, y) \partial_{\nu_c} \tilde{u}^s(y)\} ds(y), \quad (35)$$

which has a weakly-singular kernel [16].

Therefore, when x approaches an observation point $x^o \in \Gamma^s$, one easily reproduces for the bounded domain Ω^s , \tilde{u}^s and $\partial_{\nu_c} \tilde{u}^s$ satisfies on Γ^s

$$\tilde{\mathcal{K}}[\tilde{u}^s](x^o) - \tilde{\mathcal{K}}_0[1](x^o) \tilde{u}^s(x^o) = \tilde{\mathcal{S}}[\partial_{\nu_c} \tilde{u}^s](x^o), \quad (36)$$

where we have defined the following boundary integral operators in a PML environment,

$$\tilde{\mathcal{S}}[\phi](x^o) = 2 \int_{\Gamma^s} \tilde{G}(x^o, y) \phi(y) ds(y), \quad (37)$$

$$\tilde{\mathcal{K}}[\phi](x^o) = 2 \int_{\Gamma^s} \partial_{\nu_c} \tilde{G}(x^o, y) \phi(y) ds(y), \quad (38)$$

$$\tilde{\mathcal{K}}_0[\phi](x^o) = 2 \int_{\Gamma^s} \partial_{\nu_c} \tilde{G}_0(x^o, y) \phi(y) ds(y). \quad (39)$$

Consequently, we get the PML-NtD operator $\tilde{\mathcal{N}} = (\tilde{\mathcal{K}} - \tilde{\mathcal{K}}_0 1)^{-1} \tilde{\mathcal{S}}$ on Γ^s , which maps $\partial_{\nu_c} \tilde{u}^s$ to \tilde{u}^s on Γ^s .

3.4 Truncating PML-NtD operator onto Γ_{AB}

Unlike the slowly decaying wave u^s , \tilde{u}^s and $\partial_{\nu_c}\tilde{u}^s$ decay exponentially at infinity so that it is reasonable to impose $\tilde{u}^s \approx 0$ and $\partial_{\nu_c}\tilde{u}^s \approx 0$ on Γ^+ ; see [2, 3] and section 4.1 below. Therefore, operators $\tilde{\mathcal{K}}$ and $\tilde{\mathcal{S}}$ in (36) can be truncated and defined onto curve Γ_{AB} only, that is, for $x^o \in \Gamma_{AB}$,

$$\tilde{\mathcal{K}}_{AB}[\tilde{u}^s](x^o) - \tilde{\mathcal{K}}_0[1](x^o)\tilde{u}^s(x^o) \approx \tilde{\mathcal{S}}_{AB}[\partial_{\nu_c}\tilde{u}^s](x^o), \quad (40)$$

where the definition of $\tilde{\mathcal{K}}_{AB}$ is the same as $\tilde{\mathcal{K}}$ in (38) but with the integral domain replaced with Γ_{AB} , etc.

However, the integral $\tilde{\mathcal{K}}_0[1]$ cannot be truncated onto Γ_{AB} since the density function is nonzero on Γ^+ . Nevertheless, it turns out that

$$\tilde{\mathcal{K}}_0[1](x^o) = -\frac{\theta^*}{\pi}, \quad (41)$$

where θ^* is the interior angle of x^o on Γ_{AB} even when x^o is in the PML; the proof will be shown in the Appendix. Unfortunately, such a formula cannot be directly used near corners of Γ_{AB} since numerical discrepancies would appear there [16]. We now discuss how to remove the integral domain Γ^+ for operator $\tilde{\mathcal{K}}_0$.

We distinguish two cases:

- (1). Suppose $x^o \in \Gamma_{CD}$. As shown in Figure 3, for the closed curve

$$\Gamma_s = \Gamma^+ \cup AC \cup Cx^o \cup x^oD \cup DB,$$

using (41), we see that

$$2 \oint_{\Gamma_s} \partial_{\nu_c} \tilde{G}_0(x^o, y) 1 ds(y) = -\angle Cx^oD/\pi, \quad (42)$$

where we note that $\angle Cx^oD$ denotes the interior angle. On the other hand, one easily sees that

$$2 \oint_{Cx^o \cup x^oD} \partial_{\nu_c} \tilde{G}_0(x^o, y) 1 ds(y) = 0, \quad (43)$$

so that

$$2 \int_{\Gamma^+ \cup AC \cup DB} \partial_{\nu_c} \tilde{G}_0(x^o, y) 1 ds(y) = -\angle Cx^oD/\pi, \quad (44)$$

where the integral in fact becomes a Riemann integral. This implies that

$$\tilde{\mathcal{K}}_0[1](x^o) = -\angle Cx^oD/\pi + \tilde{\mathcal{K}}_{0,CD}[1](x^o),$$

$$= -\angle Cx^oD/\pi + \mathcal{K}_{0,CD}[1](x^o), \quad (45)$$

where the subscript CD indicates that the integral domain is Γ_{CD} , and the second equality holds since the integral domain is outside the PML. Furthermore, since the integrated domain is outside the PML, one easily gets [16]

$$\tilde{\mathcal{K}}_0[1](x^o) = -\angle Ax^oB/\pi + \mathcal{K}_{0,AB}[1](x^o). \quad (46)$$

We remark that (46) is more stable than (45) since x^o is sufficiently far away from A and B .

- (2). Suppose $x^o \in AC \cup DB$. Since now x^o corresponds to a smooth point of Γ_{AB} and since it is sufficiently far away from potential corners of Γ_{CD} , we can directly use the exact formula (41) that $\tilde{\mathcal{K}}_0[1](x^o) = -1$.

After the truncation, the BIE (40) only depends on the bounded curve Γ_{AB} . Therefore, by properly discretizing $\tilde{\mathcal{K}}_{AB}$, $\tilde{\mathcal{S}}_{AB}$, and $\mathcal{K}_{0,AB}$, we are able to approximate the PML-NtD operator $\tilde{\mathcal{N}}$ on Γ_{AB} now.

4 Numerical implementation

Suppose the piecewise smooth and open curve Γ_{AB} is parameterized by $x(s) = \{(x_1(s), x_2(s)) | 0 \leq s \leq L\}$, where s is the arclength. Since Γ_{AB} possibly contains corners, to smoothen the non-differentiable $x(s)$, we construct a scaling function $s = w(t)$, $0 \leq t \leq 1$ following [11], whose derivatives vanish at corners up to order p . For example, for a smooth segment of Γ_{AB} corresponding to $s \in [s^0, s^1]$ and $t \in [t^0, t^1]$ such that $s^l = w(t^l)$ for $l = 0, 1$ correspond to two corners, we may take

$$s = w(t) = \frac{s^0 w_1^p + s^1 w_2^p}{w_1^p + w_2^p}, \quad t \in [t^0, t^1], \quad (47)$$

where

$$w_1 = \left(\frac{1}{2} - \frac{1}{p} \xi^3 \right) + \frac{\xi}{p} + \frac{1}{2}, \quad w_2 = 1 - w_1, \quad \xi = \frac{2t - (t^0 + t^1)}{t^1 - t^0}.$$

Assume that $t \in [0, 1]$ is uniformly sampled by an even number, denoted by N , of grid points $\{t_j = jh\}_{j=1}^N$ with grid size $h = 1/N$, and that the grid points contain those corner points. The scaling function $s = w(t)$ creates a graded mesh on Γ_{AB} in the sense that it makes part of grid points cluster around corners while keeping the other part almost uniformly spaced [11].

We shall discuss numerically discretizing the integral operators $\tilde{\mathcal{K}}_{AB}$, $\tilde{\mathcal{S}}_{AB}$, and $\mathcal{K}_{0,AB}$ on Γ_{AB} in this section. To simplify the notations, we use $x(t)$ to denote $x(w(t))$, and use $x'(t)$ to denote $\frac{dx}{ds}(w(t))w'(t)$.

4.1 Setup of the PML

Once reparameterized by parameter t , $x(t)$ now becomes at least a C^p -class function and we can expect that integrands in (40) are sufficiently smoothed near corners. However, as Γ_{AB} overlaps with the PML, if σ_1 in (23) is not properly chosen, those integrands could have weaker regularities at the entrance points C and D , as shown in Figure 3, since $\tilde{x}_1(x_1)$ may not be smooth there. We remark here that we do not need to specify σ_2 since Γ_{AB} is far away from the horizontal PML regions parallel to x_1 .

To ensure that $\tilde{x}_1(x_1)$ is at least a C^p -class function like $x_1(t)$ at C and D , we require that derivatives of σ_1 vanishes at the entrances up to order \tilde{p} ; to be on the safe side, we choose $\tilde{p} = p + 2$. This motivates us to use a function similar to the scaling function w in (47) to construct σ_1 . Suppose the PML on Γ is defined by $\{(x_1, 0) | a_1 \leq |x_1| \leq a_1 + T\}$ where T denotes the thickness of the PML. Then, for $x_1 \in [a_1, a_1 + T]$, we take

$$\sigma_1(x_1) = \frac{0\tilde{w}_1^{\tilde{p}} + 2ST\tilde{w}_2^{\tilde{p}}}{\tilde{w}_1^{\tilde{p}} + \tilde{w}_2^{\tilde{p}}}, \quad x_1 \in [a_1, a_1 + T], \quad (48)$$

where

$$\tilde{w}_1 = \left(\frac{1}{2} - \frac{1}{\tilde{p}}\xi^3 \right) + \frac{\xi}{\tilde{p}} + \frac{1}{2}, \quad \tilde{w}_2 = 1 - \tilde{w}_1, \quad \xi = \frac{2x_1 - (a_1 + T)}{T}.$$

It is not hard to show that σ_1 bijectively maps $[a_1, a_1 + T]$ to $[0, ST]$, and satisfies the desired property at $x = a_1$. When $x_1 \in [-a_1 - T, -a_1]$, one defines $\sigma_1(x_1) = \sigma_1(-x_1)$.

Now we show how the PML absorbs an outgoing wave. Consider on $\{(x_1, 0) | x_1 > a_1\}$, a simple outgoing wave $f^s(x) = e^{icx_1}$ for a given $c > 0$ as $x_1 \rightarrow \infty$. In the PML, we obtain

$$\tilde{f}^s(x) = f^s(\tilde{x}) = e^{ic\tilde{x}_1} = e^{icx_1} e^{-c \operatorname{imag}(\tilde{x}_1)}, \quad (49)$$

where

$$\operatorname{imag}(\tilde{x}_1) = \int_{a_1}^{x_1} \sigma_1(t) dt.$$

Clearly, a larger S produces a larger σ_1 so that the imaginary part of \tilde{x}_1 becomes larger, and therefore $\tilde{f}^s(x)$ decays more quickly and is absorbed more completely at the boundary $x_1 = a_1 + T$ of the PML. We will refer to S as the absorbing magnitude of the PML in the following.

On the other hand, effectiveness of the PML is also closely related to the magnitude of c ; the greater c is, the more effective the PML becomes. In general, our unknown outgoing wave $u^s(x)$ restricted on Γ contains many

such simple outgoing functions $f^s(x)$ but with different values of c . One way to increase the smallest value of c among those simple outgoing functions, is to place the PML sufficiently far away from the local perturbation curve P . Empirically, for a plane incident wave, the distance between the PML and curve P can be around one wavelength; for a cylindrical wave due to a source x^* , it is safer to place the PML at least one wavelength away from curve P as well as the point source x^* .

4.2 Discretizing $\tilde{\mathcal{S}}_{AB}$

According to its definition, $\tilde{\mathcal{S}}_{AB}$ acting on $\partial_{\nu_c} \tilde{u}^s$ at $x = x(t_l)$, $l = 1, \dots, N$ can be parameterized by

$$\tilde{\mathcal{S}}_{AB}[\partial_{\nu_c} \tilde{u}^s](x(t_l)) = \int_0^1 S(t_l, t) \phi(t) dt, \quad (50)$$

where

$$S(t_l, t) = \frac{i}{2} H_0^{(1)}(k_0 n \text{dist}(t_l, t)), \quad (51)$$

$$\text{dist}(t_l, t) = \rho(x(t_l), x(t)), \quad (52)$$

$$\phi(t) = \partial_{\nu_c} \tilde{u}^s(x(t)) |x'(t)|. \quad (53)$$

Clearly, $\partial_{\nu_c} \tilde{u}^s$ is not continuous on Γ_{AB} since ν_c is discontinuous at corners. However, since $x'(t)$ vanishes at corners, the scaled co-normal derivative $\phi(t)$ is smoothened.

One way to discretize the integral in (50) is using the kernel splitting technique developed in [11]. Specifically, the logarithmic singularity of S at $t = t_l$ can be splitted out in terms of

$$S(t_l, t) = S_1(t_l, t) \log(4 \sin^2(\pi(t_l - t))) + S_2(t_l, t),$$

where for $t \neq t_l$, we have

$$S_1(t_l, t) = -\frac{1}{2\pi} J_0(k_0 n \rho(x(t_l), x(t))). \quad (54)$$

However, such a technique loses high accuracy when the argument of J_0 in (54) becomes complex. Specifically, if $x(t_l)$ or $x(t)$ is in the PML, $\rho(x(t_l), x(t))$ may have large imaginary part, giving rise to a blow up function J_0 and hence inducing numerical instabilities.

Fortunately, to treat integrands with logarithmic singularities, Alpert [1] developed an efficient quadrature rule which does not require a kernel splitting

process. Following such an approach, we may discretize the integral in (50) as

$$\begin{aligned}
\tilde{\mathcal{S}}_{AB}[\partial_{\nu_c} \tilde{u}^s](x(t_l)) &\approx \sum_{k=1}^{K_1} \gamma_k h [S(t_l, t_l + \delta_k h) \phi(t_l + \delta_k h) \\
&\quad + S(t_l, t_l + 1 - \delta_k h) \phi(t_l + 1 - \delta_k h)] \\
&\quad + \sum_{k=K_2}^{N-K_2} h S(t_l, t_l + t_k) \phi(t_l + t_k) \\
&= \sum_{k=1}^{K_1} \gamma_k h [S(t_l, t_l + \delta_k h) \phi(t_l + \delta_k h) \\
&\quad + S(t_l, t_l - \delta_k h) \phi(t_l - \delta_k h)] \\
&\quad + \sum_{k=K_2}^{N-K_2} h S(t_l, t_{\text{mod}(l+k, N)}) \phi(t_{\text{mod}(l+k, N)}), \tag{55}
\end{aligned}$$

where values of K_1 , K_2 , γ_k , and δ_k depend on the order of Alpert's quadrature rule and can be precomputed. For example, in a 6-th order quadrature formula, we have $K_1 = 5$ and $K_2 = 3$; the associated $\{\delta_k, \gamma_k\}_{k=1}^5$ are given in Table 1.

k	δ_k	γ_k
1	4.00488 41949 26570 E-03	1.67187 96911 47102 E-02
2	7.74565 53733 36686 E-02	1.63695 83714 47360 E-01
3	3.97284 99935 23248 E-01	4.98185 65697 70637 E-01
4	1.07567 33529 15104 E+00	8.37226 62455 78912 E-01
5	2.00379 69271 11872 E+00	9.84173 08440 88381 E-01

Table 1: The 6-th order Alpert's quadrature rule.

On the other hand, for sufficiently large p , it is reasonable to regard $\phi(t)$ as a smooth periodic function so that we may approximate ϕ by its trigonometric interpolation [32]

$$\phi(t) \approx \sum_{j=1}^N \phi(t_j) L(t - t_j), \tag{56}$$

where $L(t) = \sin(N\pi t)/[N \tan(\pi t)]$ is the Sinc function, satisfying $L(t_j) = 0$ for $1 \leq j < N$ and $L(1) = L(0) = 1$. Utilizing (56), we may rewrite equation

(55) in terms of $\phi(t_j)$ for $1 \leq j \leq N$ so that we obtain an $N \times N$ matrix \mathbf{S} that satisfies

$$\tilde{\mathcal{S}}_{AB}[\partial_{\nu_c} \tilde{u}^s] \begin{bmatrix} x(t_1) \\ \vdots \\ x(t_N) \end{bmatrix} \approx \mathbf{S} \begin{bmatrix} \phi(t_1) \\ \vdots \\ \phi(t_N) \end{bmatrix}, \quad (57)$$

where the left-hand side represents a column vector produced by evaluating $\tilde{\mathcal{S}}_{AB}[\partial_{\nu_c} \tilde{u}^s]$ at each element $x(t_j)$ of the column vector for $1 \leq j \leq N$.

4.3 Discretizing $\tilde{\mathcal{K}}_{AB}$

According to its definition, $\tilde{\mathcal{K}}_{AB}$ acting on \tilde{u}^s at $x = x(t_l)$ can be parameterized as

$$\tilde{\mathcal{K}}_{AB}[\tilde{u}^s](x(t_l)) = \int_0^1 K(t_l, t)g(t)dt, \quad (58)$$

where

$$K(t_l, t) = -\frac{ik_0 n}{2} \frac{\kappa(t_l, t)}{\text{dist}(t_l, t)} H_1^{(1)}(k_0 n \text{dist}(t_l, t)), \quad (59)$$

$$\kappa(t_l, t) = \tilde{x}'_2(t)(\tilde{x}_1(t) - \tilde{x}_1(t_l)) - \tilde{x}'_1(t)(\tilde{x}_2(t) - \tilde{x}_2(t_l)), \quad (60)$$

$$g(t) = \tilde{u}^s(x(t)). \quad (61)$$

Thus, similar to operator $\tilde{\mathcal{S}}_{AB}$, by applying Alpert's quadrature rule, we discretize the integral in (58) as

$$\begin{aligned} \tilde{\mathcal{K}}_{AB}[\tilde{u}](x(t_l)) &\approx \sum_{k=1}^{K_1} \gamma_k h [K(t_l, t_l + \delta_k h)g(t_l + \delta_k h) \\ &\quad + K(t_l, t_l - \delta_k h)g(t_l - \delta_k h)] \\ &\quad + \sum_{k=K_2}^{N-K_2} h K(t_l, t_{\text{mod}(l+k, N)})g(t_{\text{mod}(l+k, N)}). \end{aligned} \quad (62)$$

By choosing p sufficiently large, we may approximate g by its trigonometric interpolation like (56) but with ϕ replaced by g . Consequently, we may rewrite equation (62) in terms of $g(t_j)$ for $1 \leq j \leq N$ so that we obtain an $N \times N$ matrix \mathbf{K} that satisfies

$$\tilde{\mathcal{K}}_{AB}[\tilde{u}^s] \begin{bmatrix} x(t_1) \\ \vdots \\ x(t_N) \end{bmatrix} \approx \mathbf{K} \begin{bmatrix} g(t_1) \\ \vdots \\ g(t_N) \end{bmatrix}. \quad (63)$$

The discretization of $\mathcal{K}_{0,AB}$ in (46) can be derived similarly.

After the discretization of $\tilde{\mathcal{S}}_{AB}$, $\tilde{\mathcal{K}}_{AB}$, and $\mathcal{K}_{0,AB}$, one obtains from (40) that

$$(\mathbf{K} - \mathbf{H})\tilde{\mathbf{u}}^s \approx \mathbf{S}\boldsymbol{\phi}, \quad (64)$$

where \mathbf{H} is a diagonal matrix with entries $\tilde{\mathcal{K}}_0[1](x(t_l))$ for $1 \leq l \leq N$,

$$\begin{aligned} \tilde{\mathbf{u}}^s &= [g(x(t_1)), \dots, g(x(t_N))]^T, \\ \boldsymbol{\phi} &= [\phi(x(t_l)), \dots, \phi(x(t_N))]^T. \end{aligned}$$

Consequently, one gets

$$\tilde{\mathbf{u}}^s \approx (\mathbf{K} - \mathbf{H})^{-1}\mathbf{S}\boldsymbol{\phi} := \mathbf{N}\boldsymbol{\phi}, \quad (65)$$

where the $N \times N$ matrix \mathbf{N} in fact approximates a scaled PML-NtD operator $\tilde{\mathcal{N}}_s$ which maps $\phi = \partial_{\nu_c} \tilde{u}^s(x)|_{x'}$ to \tilde{u}^s on Γ_{AB} .

4.4 A stabilizing technique

Clearly, to make the approximations of $\tilde{\mathcal{S}}_{AB}$ and $\tilde{\mathcal{K}}_{AB}$ accurate enough, a high order quadrature rule and a large scaling parameter p are always preferable; otherwise, one needs a sufficiently large N . Suppose we desire a 6-th order of accuracy so that nodes and weights of Alpert's quadrature rule are chosen based on Table 1. To be consistent, we choose $p = 6$ in the scaling function $s = w(t)$. Under such a circumstance, when computing the kernel functions $S(t_l, t)$ and $K(t_l, t)$, we observe that $|t_l - t|$ can be as small as $\delta_1 h = O(\frac{10^{-3}}{N})$. When t_l is close to a corner point, the physical distance $\text{dist}(t_l, t)$ can be further shrunk to $O(\frac{10^{-3p}}{N^p}) = O(\frac{10^{-18}}{N^6})$ by the scaling function. Unfortunately, even for a coarse mesh, this can be less than or close to the round-off error $O(10^{-16}x(t_l))$ in the computation of $\text{dist}(t_l, t)$. In such a situation, $\text{dist}(t_l, t)$ is simply regarded as 0 in a double-precision computation. Consequently, division by zero occurs in the computation of $S(t_l, t)$ and $K(t_l, t)$ when t is close to t_l and when t_l is close to a corner.

To resolve this instability issue, one approach is to reduce the accuracy order to $p = 3$ or less. However, this can make the total computational process extremely inefficient in practice. In this section, we develop numerical techniques which can accurately compute $S(t_l, t)$ and $K(t_l, t)$ when t is close to t_l and t_l is close to a corner.

Observing their expressions (51) and (60), the instability issue comes from the two terms $\text{dist}(t_l, t)$ and $\kappa(t_l, t)$ since they involve subtractions of two extremely close quantities. We discuss $\text{dist}(t_l, t)$ first.

Without loss of generality, we assume $t > t_l$, so that $\tilde{x}(\xi), \xi \in [t_l, t]$ becomes a piecewise smooth function; note that here $\tilde{x}(\xi)$ may meet some corner. At first, we assume that \tilde{x} on $[t_l, t]$ is smooth.

To preserve enough significant digits, we require accurately computing

$$\tilde{x}_i(t) - \tilde{x}_i(t_l), \quad (66)$$

for $i = 1, 2$. There are two approaches to realize this. The first approach is to use the Taylor series of \tilde{x}_i at t_l , that is,

$$\tilde{x}_i(t) - \tilde{x}_i(t_l) = \sum_{j=1}^{\infty} \frac{\tilde{x}_i^{(j)}(t_l)}{j!} (t - t_l)^j. \quad (67)$$

Unfortunately, this approach is ineffective since it is not easy to control the truncation error and since we require the computation of many high order derivatives. The second and more effective approach utilizes the Newton-Lebnitz formula, rewriting (66) in the form,

$$\begin{aligned} \tilde{x}_i(t) - \tilde{x}_i(t_l) &= \tilde{x}_i(w(t)) - \tilde{x}_i(w(t_l)) \\ &= \int_0^{w(t)-w(t_l)} \frac{d\tilde{x}_i}{ds}(w(t_l) + s) ds, \\ &= \int_0^{\int_{t_l}^t w'(\tau) d\tau} \frac{d\tilde{x}_i}{ds}(w(t_l) + s) ds. \end{aligned} \quad (68)$$

for $i = 1, 2$. Such an representation gives rise to significant advantages. Specifically, the integrand in the primary integral is an $O(1)$ quantity so that using numerical integrations (e.g., Gaussian quadrature rules), to compute the integral can highly reduce round-off errors; moreover, we only require the first-order derivative of \tilde{x}_i to obtain accurate result. To ensure stability, the upper limit is also rewritten as an integral form. Consequently, $\text{dist}(t_l, t)$ can be evaluated via

$$\text{dist}(t_l, t) = \sqrt{\sum_{i=1}^2 \left(\int_0^{\int_{t_l}^t w'(\tau) d\tau} \frac{d\tilde{x}_i}{ds}(w(t_l) + s) ds \right)^2}. \quad (69)$$

We remark that the aim of using arclength s but not the grading parameter t as the integral variable is to further stabilize the involved computations since integrands roughly become $O(1)$ quantities.

Next, we discuss the computation of

$$\begin{aligned} \kappa(t_l, t) &= w'(t) \left[\frac{d\tilde{x}_2}{ds}(w(t)) (\tilde{x}_1(w(t)) - \tilde{x}_1(w(t_l))) \right. \\ &\quad \left. - \frac{d\tilde{x}_1}{ds}(w(t)) (\tilde{x}_2(w(t)) - \tilde{x}_2(w(t_l))) \right] \end{aligned}$$

$$:=w'(t)\bar{\kappa}(t_l, t). \quad (70)$$

Using Newton-Lebnitz formula, we may rewrite $\bar{\kappa}(t_l, t)$ as

$$\begin{aligned} \bar{\kappa}(t_l, t) &= \int_0^{w(t)-w(t_l)} \left[\frac{d^2\tilde{x}_2}{ds^2}(w(t_l) + s) (\tilde{x}_1(w(t_l) + s) - \tilde{x}_1(w(t_l))) \right. \\ &\quad \left. - \frac{d^2\tilde{x}_1}{ds^2}(w(t_l) + s) (\tilde{x}_2(w(t_l) + s) - \tilde{x}_2(w(t_l))) \right] ds \\ &= \int_0^{\int_{t_l}^t w'(\tau)d\tau} \int_0^s \left[\frac{d^2\tilde{x}_2}{ds^2}(w(t_l) + s) \frac{d\tilde{x}_1}{ds}(w(t_l) + \eta) \right. \\ &\quad \left. - \frac{d^2\tilde{x}_1}{ds^2}(w(t_l) + s) \frac{d\tilde{x}_2}{ds}(w(t_l) + \eta) \right] d\eta ds. \end{aligned} \quad (71)$$

Using numerical integrations to compute the above double integrals can yield accurate results.

Now, suppose that $\tilde{x}(\xi), \xi \in [t_l, t]$ contains a corner at $\xi = t^* \in (t_l, t)$. Since $\tilde{x}(\xi)$ consists of two smooth segments corresponding to $[t_l, t^*]$ and $[t^*, t]$, respectively, the following splitting

$$\tilde{x}_i(t) - \tilde{x}_i(t_l) = (\tilde{x}_i(t) - \tilde{x}_i(t^*)) + (\tilde{x}_i(t^*) - \tilde{x}_i(t_l)), \quad (72)$$

indicates that Newton-Lebnitz formula is applicable for either term on the right-hand side so that numerical integrations can still offer an accurate result for $\text{dist}(t_l, t)$.

As for $\kappa(t_l, t)$, we have

$$\begin{aligned} \bar{\kappa}(t_l, t) &= \bar{\kappa}(t_l, t^*) + \bar{\kappa}(t^*, t) \\ &+ \left[\left(\frac{d\tilde{x}_2}{ds}(w(t)) - \frac{d\tilde{x}_2}{ds}(w(t^*+)) \right) (\tilde{x}_1(w(t^*)) - \tilde{x}_1(w(t_l))) \right. \\ &\quad \left. - \left(\frac{d\tilde{x}_1}{ds}(w(t)) - \frac{d\tilde{x}_1}{ds}(w(t^*+)) \right) (\tilde{x}_2(w(t^*)) - \tilde{x}_2(w(t_l))) \right] \\ &+ \left[\left(\frac{d\tilde{x}_2}{ds}(w(t^*+)) - \frac{d\tilde{x}_2}{ds}(w(t^*-)) \right) (\tilde{x}_1(w(t^*)) - \tilde{x}_1(w(t_l))) \right. \\ &\quad \left. - \left(\frac{d\tilde{x}_1}{ds}(w(t^*+)) - \frac{d\tilde{x}_1}{ds}(w(t^*-)) \right) (\tilde{x}_2(w(t^*)) - \tilde{x}_2(w(t_l))) \right] \\ &= \bar{\kappa}(t_l, t^*) + \bar{\kappa}(t^*, t) \\ &+ \int_0^{\int_{t^*}^t w'(\tau)d\tau} \int_0^{\int_{t_l}^{t^*} w'(\tau)d\tau} \left[\frac{d^2\tilde{x}_2}{ds^2}(w(t^*) + s) \frac{d\tilde{x}_1}{ds}(w(t_l) + \eta) \right. \\ &\quad \left. - \frac{d^2\tilde{x}_1}{ds^2}(w(t^*) + s) \frac{d\tilde{x}_2}{ds}(w(t_l) + \eta) \right] d\eta ds \end{aligned}$$

$$\begin{aligned}
& + \left[\left(\frac{d\tilde{x}_2}{ds}(w(t^*+)) - \frac{d\tilde{x}_2}{ds}(w(t^*-)) \right) \int_0^{\int_{t_l}^{t_l^*} w'(\tau) d\tau} \frac{d\tilde{x}_1}{ds}(w(t_l) + \eta) d\eta \right. \\
& \left. - \left(\frac{d\tilde{x}_1}{ds}(w(t^*+)) - \frac{d\tilde{x}_1}{ds}(w(t^*-)) \right) \int_0^{\int_{t_l}^{t_l^*} w'(\tau) d\tau} \frac{d\tilde{x}_2}{ds}(w(t_l) + \eta) d\eta \right],
\end{aligned} \tag{73}$$

where (t^*+) and (t^*-) indicate limits are taken from right side and left side, respectively. Clearly, all the four terms on the right-hand side can be accurately evaluated through numerical integrations.

5 Wave field evaluations

Suppose now in each domain Ω_j , we have obtained an $N \times N$ matrices \mathbf{N}_j to approximate the scaled NtD operator $\tilde{\mathcal{N}}_{s,j}$, mapping $|x'| \partial_{\nu_c} \tilde{u}_j^s$ to \tilde{u}_j^s on Γ_{AB} , for $j = 1, 2$. Then

$$\mathbf{N}_j \phi_j = \tilde{\mathbf{u}}_j^s, \tag{74}$$

where

$$\begin{aligned}
\tilde{\mathbf{u}}_j^s &= [\tilde{u}_j^s(x(t_1)), \dots, \tilde{u}_j^s(x(t_N))]^T, \\
\phi_j &= [|x'(t_1)| \partial_{\nu_c} \tilde{u}_j^s(x(t_1)), \dots, |x'(t_N)| \partial_{\nu_c} \tilde{u}_j^s(x(t_N))]^T.
\end{aligned}$$

According to the transmission conditions (9) and (10), the complexified outgoing wave \tilde{u}_j^s , at the N grid points on Γ_{AB} , satisfies

$$\tilde{\mathbf{u}}_1^s - \tilde{\mathbf{u}}_2^s = \mathbf{b}_1, \tag{75}$$

$$\eta_1 \phi_1 - \eta_2 \phi_2 = \mathbf{b}_2, \tag{76}$$

where we have defined

$$\begin{aligned}
\mathbf{b}_1 &= [-[\tilde{u}_0^{tot}](x(t_1)), \dots, -[\tilde{u}_0^{tot}](x(t_N))]^T, \\
\mathbf{b}_2 &= [-|x'(t_1)| [\eta_j \partial_{\nu_c} \tilde{u}_0^{tot}](x(t_1)), \dots, -|x'(t_N)| [\eta_j \partial_{\nu_c} \tilde{u}_0^{tot}](x(t_N))]^T.
\end{aligned}$$

Thus, by (74), we obtain

$$\begin{bmatrix} \mathbf{N}_s^1 & -\mathbf{N}_s^2 \\ \eta_1 \mathbf{I} & -\eta_2 \mathbf{I} \end{bmatrix} \begin{bmatrix} \phi_1 \\ \phi_2 \end{bmatrix} = \begin{bmatrix} \mathbf{b}_1 \\ \mathbf{b}_2 \end{bmatrix}, \tag{77}$$

which can be solved by

$$\begin{bmatrix} \phi_1 \\ \phi_2 \end{bmatrix} = \begin{bmatrix} \mathbf{N}_s^1 & -\mathbf{N}_s^2 \\ \eta_1 \mathbf{I} & -\eta_2 \mathbf{I} \end{bmatrix}^{-1} \begin{bmatrix} \mathbf{b}_1 \\ \mathbf{b}_2 \end{bmatrix}, \tag{78}$$

or equivalently,

$$\boldsymbol{\phi}_1 = (\mathbf{N}_s^1 - \frac{\eta_1}{\eta_2} \mathbf{N}_s^2)^{-1} (\eta_2^{-1} \mathbf{N}_s^2 \mathbf{b}_2 + \mathbf{b}_1), \quad (79)$$

$$\boldsymbol{\phi}_2 = \frac{\eta_1}{\eta_2} \boldsymbol{\phi}_1 - \frac{\mathbf{b}_2}{\eta_2}. \quad (80)$$

Consequently, we obtain $\tilde{\mathbf{u}}_j^s = \mathbf{N}_j \boldsymbol{\phi}_j$ on Γ_{AB} .

As for any point $x \in \Omega_j$, we may directly use (30) to compute $\tilde{u}_j^s(x)$, that is

$$\tilde{u}_j^s(x) \approx \int_{\Gamma_{AB}} \{ \partial_{\nu_c} \tilde{G}_j(x, y) \tilde{u}_j^s(y) - \tilde{G}_j(x, y) \partial_{\nu_c} \tilde{u}_j^s(y) \} ds(y), \quad (81)$$

where we keep curve Γ_{AB} only since both $\tilde{u}_j^s(y)$ and $\partial_{\nu_c} \tilde{u}_j^s(y)$ approximately are 0 on $\tilde{\Gamma}/\Gamma_{AB}$. After parameterized by the scaling function $s = w(t)$ in (47), the integrand in (81) becomes periodic and smooth so that by trapezoidal rule, we may approximate

$$\begin{aligned} \tilde{u}_j^s(x^o) \approx \frac{1}{N} \sum_{l=1}^N & \left[\partial_{\nu_c} \tilde{G}_j^s(x^o, x(t_l)) |x'(t_l)| \tilde{u}_j^s(x(t_l)) \right. \\ & \left. - \tilde{G}_j^s(x^o, x(t_l)) |x'(t_l)| \partial_{\nu_c} \tilde{u}_j^s(x(t_l)) \right]. \end{aligned} \quad (82)$$

Therefore, in the domain outside the PML, we obtain $u_j^s = \tilde{u}_j^s$ so that the total wave field $u^{tot} = u^s + u_0^{tot}$.

6 Numerical examples

In this section, we will carry out several numerical experiments to illustrate the proposed methodology. In all examples, the physical region is defined as $\{(x_1, x_2) | |x_1| \leq a_1, a_1 > 0\}$, while the PML region is defined as $\{(x_1, x_2) | a_1 \leq |x_1| \leq a_1 + T, a_1 > 0, T > 0\}$ with thickness T . Therefore, the truncated interface Γ_{AB} is just Γ restricted on $x_1 \in [-a_1 - T, a_1 + T]$, while the physical region on Γ_{AB} , denoted by Γ_P below, is just Γ restricted on $x_1 \in [-a_1, a_1]$. To achieve a high-order accuracy, we take $p = 6$ in the scaling function $s = w(t)$ associated with the 6-th order Alpert's quadrature rule, using nodes and weights defined in Table 1. We will mainly consider TM-polarization problems.

6.1 Example 1: Perfectly flat surface

To validate our method, the first example is a perfectly flat surface $\Gamma = \{(x_1, x_2) | x_2 = 0\}$, where $n_1 = 1$, $n_2 = 2$, and the freespace wavelength $\lambda = 1$

so that $k_0 = 2\pi$. When u^{inc} represents a plane incident wave, $u^{tot} = u_0^{tot}$ in (5) is the exact solution, making $u^s = 0$ in both Ω_1 and Ω_2 . To avoid such trivial solutions, we here test the case when u^{inc} is a cylindrical wave due to a point source $x^* = (0, 0.1)$, so that u^{tot} represents a layered Green's function at x^* .

In the implementation, although Γ is smooth, we still set $(0, 0)$ as an artificial corner since it is close to the source x^* . As shown in [25], an explicit expression of the layered Green's function is available so that we can obtain the exact solution u_{exa}^{tot} for reference.

Taking $N = 400$, $a_1 = 1$ and $T = 1$, we compute \tilde{u}^{tot} , and compare it with the exact solution u_{exa}^{tot} on Γ_{AB} , as shown in Figure 4. Clearly, on Γ_P , \tilde{u}^{tot} and

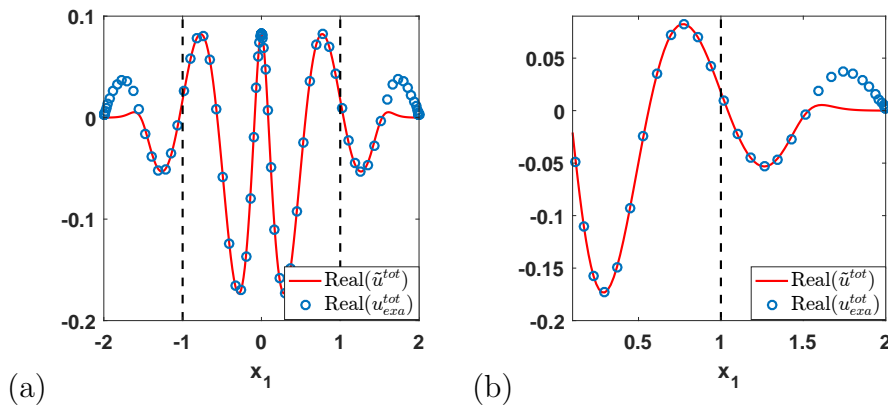


Figure 4: Example 1: real parts of \tilde{u}^{tot} and the exact solution u_{exa}^{tot} on: (a) $x_1 \in [-1, 1]$; (b) $x_1 \in [0.3, 1]$. Dashed lines indicate entrances of the PML.

u_{exa}^{tot} coincide very well; in the PML region corresponding to $|x_1| \in [1, 2]$, \tilde{u}^{tot} decay quickly to 0 and u_{exa}^{tot} still oscillates with a slowly decaying amplitude, as what we are expecting. Figure 5 show numerical and exact solutions of the real part of u^{tot} in a box $[-1, 1] \times [-1, 1]$, where Figure 5(a) is based on a numerical solution using $N = 400$ grid points on Γ_{AB} . Obviously, they coincide with each other quite well.

To illustrate the order of accuracy, we study numerical error of u^{tot} on Γ_P against the number of grid points N in discretizing Γ_{AB} when $S = 1$. Since grid points vary for different values of N , we choose to evaluate u^{tot} at grid points on Γ_P when $N = 20$, referred to as a reference set of points, to realize the comparison; for $N \neq 20$, we just interpolate the numerical solution onto the reference set of points by (56). Using the exact solution u_{exa}^{tot} as a reference solution, we compute numerical errors for different values of N , as depicted in Figure 6(a), where the vertical axis represents the relative error,

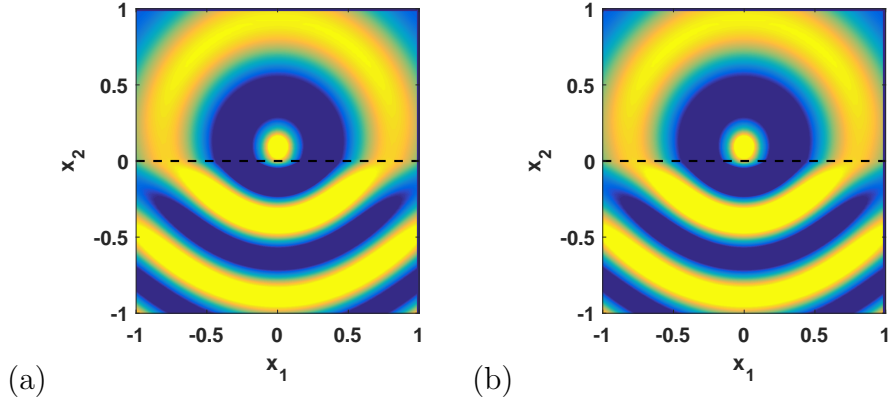


Figure 5: Example 1: real part of u^{tot} on $[-1, 1] \times [-1, 1]$. (a) numerical solution; (b) exact solution. Dashed line indicates location of Γ .

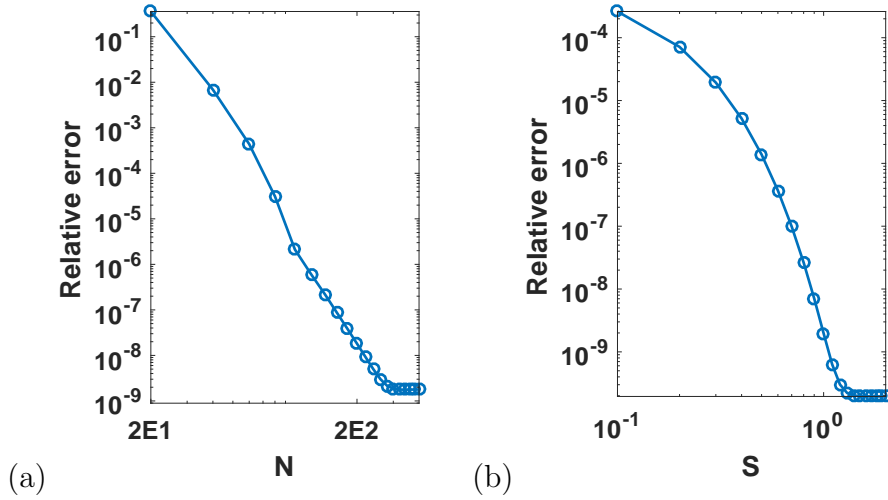


Figure 6: Example 1: Using the exact solution as a reference solution: (a) numerical error of u^{tot} on Γ_P against total number of points N when $S = 1$; (b) numerical error of u^{tot} on Γ_P against the absorbing magnitude S when $N = 400$.

the horizontal axis represents N , and both axes are logarithmically scaled. Clearly, slope of the decaying part of the curve reveals that our method exhibits at least a seventh-order accuracy.

To illustrate that our PML effectively terminates the outgoing wave, we now fix $N = 400$ and compute u^{tot} at grid points on Γ_P for different values of S , ranging from 0.1 to 2; the grid points now are independent of S . Using

the exact solution u_{exa}^{tot} as a reference solution, we compute relative errors for different values of S , as shown in Figure 6(b), where both axes are logarithmically scaled. We observe that the relative error decays exponentially at the beginning for S in a range of small values, and however it terminates for larger S . We remark that to maintain an exponentially decaying error for larger S , one has to choose larger N to increase the number of points in the PML and to decrease the discretization error. From Figure 6, we easily see that the numerical solution for $N = 400$ and $S = 1$ attains eight significant digits.

To conclude this example, we observe that numerical accuracy in fact can be improved by two approaches: increasing N and increasing S . When exact solution is not available, it is reasonable that one combines the convergence curve of relative error against N for a fixed S , and the convergence curve of relative error against S for a fixed N to truly discover how accurate the solution has obtained, as will be shown below.

6.2 Example 2: Two semicircles

In the second example, we consider a local perturbation that consists of two connected semicircles of radius 1; the interface is shown as dotted line in Figure 7. Suppose again $n_1 = 1$, $n_2 = 2$ and $k_0 = 2\pi$ with wavelength $\lambda = 1$. We consider two incident waves:

- (i) a plane incident wave with incident angle $\alpha = \frac{\pi}{3}$;
- (ii) a cylindrical wave due to point source $x^* = (1, 1)$.

In the implementation, we take $a_1 = 2.5$ and $T = 1$ so that Γ_P becomes $\{(x_1, x_2) | -2.5 \leq x_1 \leq 2.5\}$ while the PML region is $\{(x_1, x_2) | 2.5 \leq |x_1| \leq 3.5\}$. The total wave field u^{tot} for the two incident waves in $[-2.5, 2.5] \times [-2.5, 2.5]$ is computed and plotted in Figure 7 (a) and (b), respectively, based on a numerical solution using $N = 1600$ grid points on Γ_{AB} .

To illustrate the order of accuracy for either incident wave, we compute numerical error of u^{tot} on Γ_P against the number of grid points N when $S = 1$. As in example 1, a reference set of points is chosen as the grid points on Γ_P when $N = 160$. The reference solution is obtained by computing u^{tot} at the reference set of points when $N = 1600$ grid points are used. Numerical results for both incident waves are shown in Figure 8, which shows that our results exhibit a seventh-order accuracy for both incident waves.

To illustrate that our PML effectively terminates the outgoing wave for each incident wave, we now fix $N = 1600$ and compute u^{tot} at grid points on Γ_P for different values of S , ranging from 0.1 to 2; the grid points now

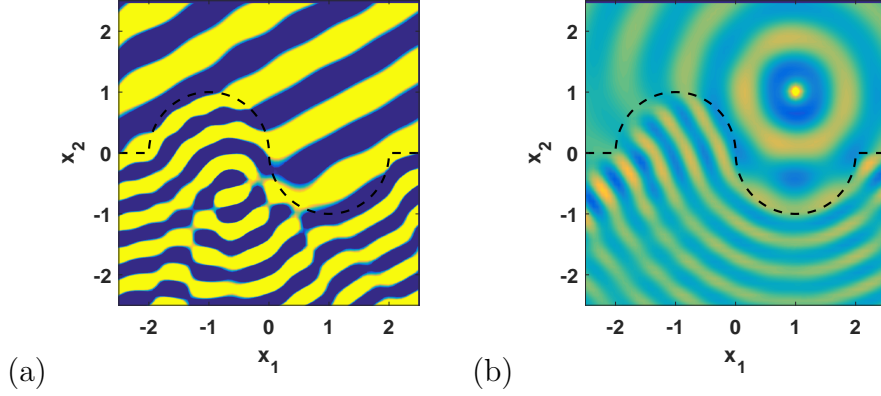


Figure 7: Example 2: real part of u^{tot} on $[-2.5, 2.5] \times [-2.5, 2.5]$. (a) plane incident wave with angle $\alpha = \frac{\pi}{3}$; (b) cylindrical wave with source $\mathbf{x}^* = (1, 1)$. Dashed line indicates location of Γ .

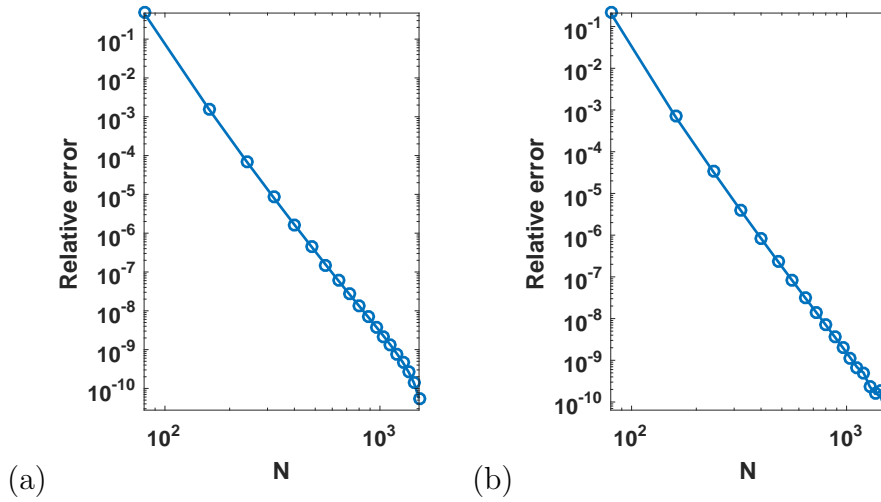


Figure 8: Example 2: numerical error of u^{tot} on Γ_P against total number of points N when $S = 1$: (a) plane incident wave with angle $\alpha = \frac{\pi}{3}$; (b) cylindrical wave due to point source $x^* = (1, 1)$.

are independent of S . Considering the numerical solution u^{tot} for $S = 2$ as a reference solution, we compute relative errors for different values of S . Numerical results are shown in Figure 9. Clearly, we observe that numerical error for each incident wave decays exponentially at the beginning when S is not very large, and then decays algebraically for larger S as N is fixed.

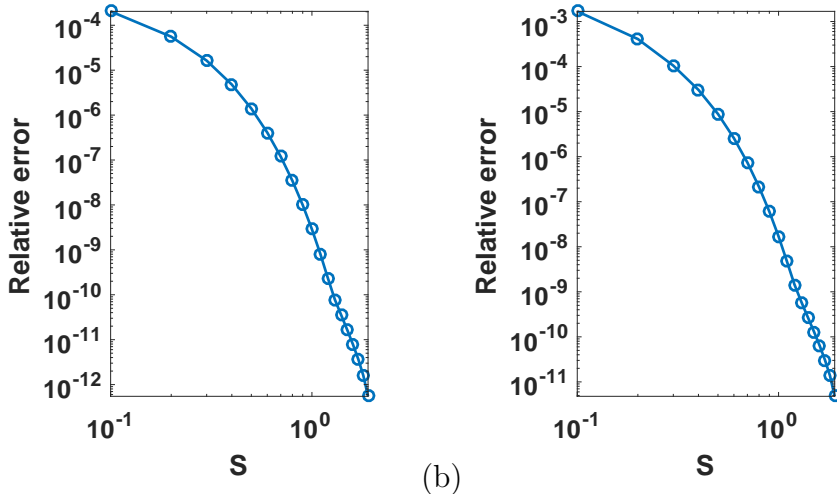


Figure 9: Example 2: numerical error of u^{tot} on $\Gamma_{\mathcal{P}}$ against the absorbing magnitude S when $N = 1600$: (a) plane incident wave with angle $\alpha = \frac{\pi}{3}$; (b) cylindrical wave due to point source $x^* = (1, 1)$.

At last, combining Figures 8(a) and 9(a), we see that our numerical solution for the plane incident wave attains eight significant digits when $N = 1600$ and $S = 1$. Similarly, combining Figures 8(b) and 9(b), we see that our numerical solution for the cylindrical incident wave attains eight significant digits when $N = 1600$ and $S = 1$.

6.3 Example 3: An obstacle above the interface

In this example, we study a more complicated structure, where an obstacle is placed above the interface. With the obstacle involved, our PML-based BIE formulation only requires an extra NtD operator defined on the boundary of the obstacle, which can be obtained by a regular BIE in physical domain as described in [16]. Then, according to transmission conditions on the obstacle and the interface, the final linear system can be obtained with ease.

Suppose refractive index of the obstacle is $n_{ob} = 2$, $n_1 = 1$, $n_2 = 3$, and $k_0 = 2\pi$ with $\lambda = 1$. The basic structure is shown in Figure 10, where a drop shape is placed one unit above the interface which contains five uniformly spaced indentations. We consider two incident waves:

- (i) a plane incident wave with incident angle $\alpha = \frac{\pi}{3}$;
- (ii) a cylindrical wave due to point source $x^* = (3, 1)$.

In the implementation, we take $a_1 = 5.5$ and $T = 1$ so that Γ_P becomes $\{(x_1, x_2) | -5.5 \leq x_1 \leq 5.5\}$, while the PML domain becomes $\{(x_1, x_2) | 5.5 \leq |x_1| \leq 6.5\}$. The total wave field u^{tot} for the two incident waves in $[-5.5, 5.5] \times [-5.5, 5.5]$ is computed and plotted in Figure 10 (a) and (b), respectively, based on a numerical solution on Γ_{AB} and the obstacle boundary Γ_{ob} , using $N = 3150$ grid points on Γ_{AB} (150 points per segment) and $N_{ob} = 800$ grid points on Γ_{ob} , the boundary of the obstacle.

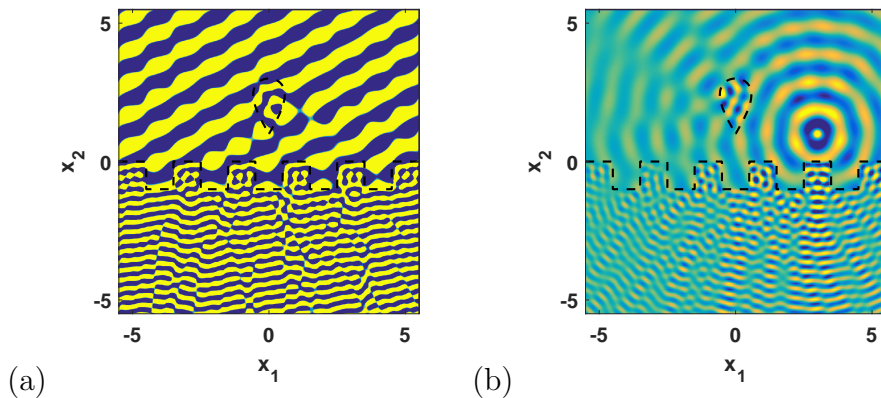


Figure 10: Example 3: real part of u^{tot} on $[-5.5, 5.5] \times [-5.5, 5.5]$: (a) plane incident wave with angle $\alpha = \frac{\pi}{3}$; (b) cylindrical plane wave with point source $x^* = (3, 1)$. Dashed line indicates location of Γ .

To illustrate the order of accuracy for either incident wave, we study numerical error of u^{tot} on Γ_P against the number of grid points N in discretizing Γ_{AB} when $S = 1$, where we fix the number of grid points on Γ_{ob} to be $N_{ob} = 800$. As in example 1, a reference set of points is chosen as the grid points on Γ_P when $N = 840$. The reference solution is obtained by computing u^{tot} at the reference set of points when $N = 3150$ grid points are used. Numerical results for both incident waves are shown in Figure 11, which shows that our results roughly exhibit a seventh-order accuracy for both incident waves.

To illustrate that our PML effectively terminates the outgoing wave for each incident wave, we now fix $N = 3150$ and compute u^{tot} at grid points on Γ_P for different values of S , ranging from 0.1 to 2; the grid points now are independent of S . Considering the numerical solution u^{tot} for $S = 2$ as a reference solution, we compute relative errors for different values of S . Numerical results are shown in Figure 12. Clearly, we observe that numerical error for each incident wave decays exponentially at the beginning when S is not very large, and then decays algebraically for larger S as N is fixed.

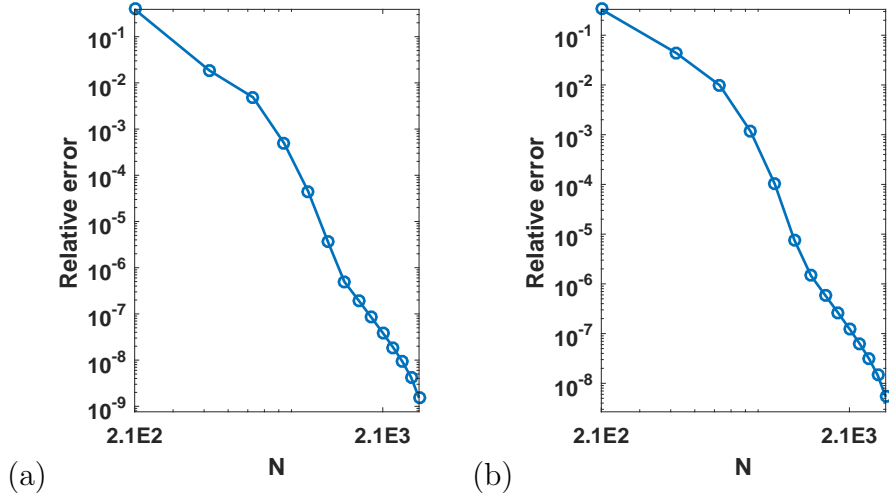


Figure 11: Example 3: numerical error of u^{tot} on Γ_P against total number of points N when $S = 1$: (a) plane incident wave with angle $\alpha = \frac{\pi}{3}$; (b) cylindrical wave due to a point source $x^* = (3, 1)$.

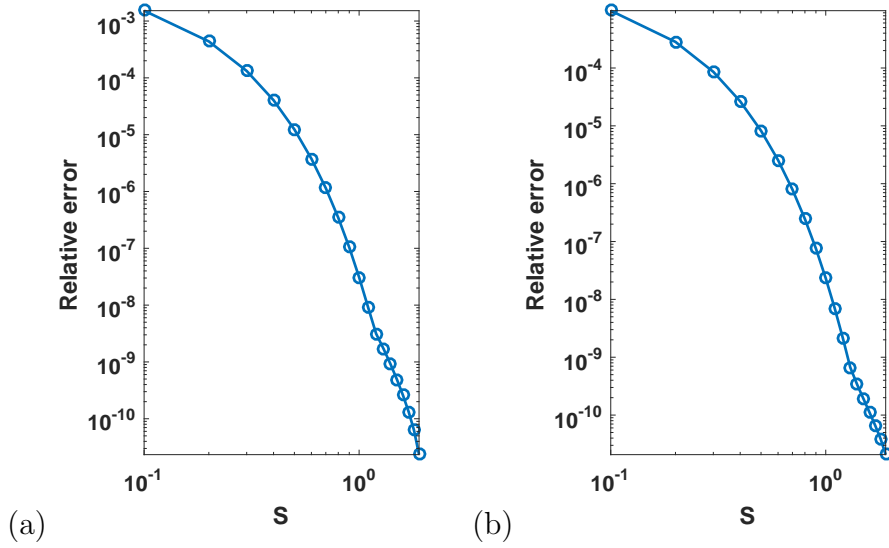


Figure 12: Example 3: numerical error of u^{tot} on Γ_P against the absorbing magnitude S when $N = 3150$: (a) plane incident wave with angle $\alpha = \frac{\pi}{3}$; (b) cylindrical wave due to a point source $x^* = (3, 1)$.

At last, combining Figures 11(a) and 12(a), we see that our numerical solution for the plane incident wave attains seven significant digits when

$N = 3150$ and $S = 1$. Similarly, combining Figures 11(b) and 12(b), we see that our numerical solution for the cylindrical incident wave attains seven significant digits when $N = 3150$ and $S = 1$.

6.4 Example 4: Interface with different elevations at infinity

In previous examples, flat part of the interface away from the local perturbation P have the same elevations at infinity. However, if the flat part has different elevations toward infinity, then all existing methods based on layered Green's function break down since now for the background layered medium, an explicit form of the layered medium Green's function in terms of Sommerfeld integrals is hard to develop. To conclude this section, we study such a challenging example.

For a plane incident wave, using a flat part on one side (left or right) to define u_0^{tot} can only suppress the reflective and transmittive waves in u^s on the same side but not on the other side, since the reflection and transmission coefficients are different on each side. Consequently, it is possible that the difference field $u^{tot} - u_0^{tot}$ is not outgoing in all directions, e.g., if u^{inc} a normal incident wave. The current PML-based BIE formulation fails in this case. We expect to address this issue in an ongoing project.

Fortunately, when u^{inc} is a cylindrical wave due to a point source, we may still use u_0^{tot} defined in (11) to construct an outgoing wave u^s such that our PML-based BIE formulation still works. To justify the methodology, we test a very simple structure where two half-lines with different elevations are connected just by a line segment of 1 unit, as shown in Figure 13, where we suppose $n_1 = 1$, $n_2 = 2$ and $k_0 = 2\pi$ with wavelength $\lambda = 1$. We consider a cylindrical incident wave due to point source $x^* = (0, 1.1)$.

In the implementation, we take $a_1 = 1$ and $T = 1$ so that Γ_P becomes $\{(x_1, x_2) | -1 \leq x_1 \leq 1\}$, while the PML domain becomes $\{(x_1, x_2) | 1 \leq |x_1| \leq 2\}$. The total wave field u^{tot} for the incident wave in $[-1, 1] \times [3, 3]$ is computed and plotted in Figure 13, based on a numerical solution using $N = 2400$ grid points on Γ_{AB} (800 points per smooth segment).

To illustrate the order of accuracy, we study numerical error of u^{tot} on Γ_P against the number of grid points N in discretizing Γ_{AB} when $S = 1$. As in example 1, a reference set of points is chosen as the grid points on Γ_P when $N = 120$. The reference solution is obtained by computing u^{tot} at the reference set of points when $N = 2400$ grid points are used. Numerical results are shown in Figure 14(a), which shows that our results roughly exhibit a fourth-order accuracy.

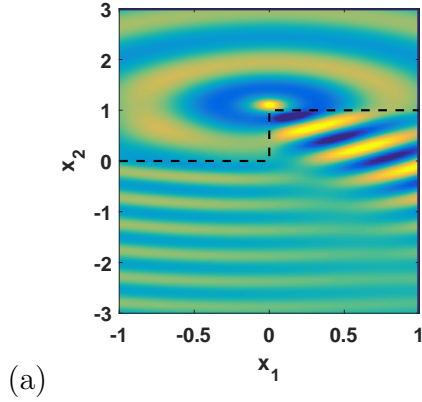


Figure 13: Example 4: real part of u^{tot} on $[-1, 1] \times [-3, 3]$ for cylindrical plane wave due to source $\mathbf{r}_0 = [0, 1.1]^T$. Dashed line indicates location of Γ .

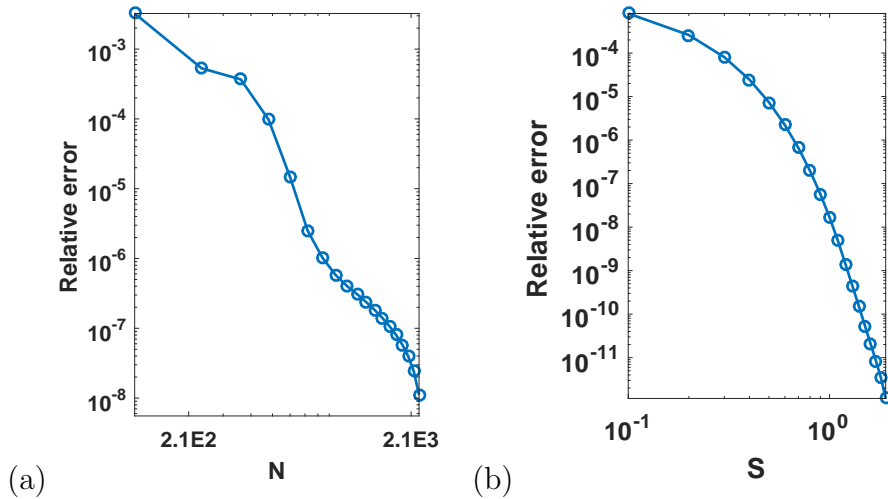


Figure 14: Example 4: (a) numerical error of u^{tot} on Γ_P against the total number of points N when $S = 1$; (b) numerical error of u^{tot} on Γ_P against the absorbing magnitude S when $N = 2400$.

To illustrate that our PML effectively terminates the outgoing wave, we now fix $N = 2400$ and compute u^{tot} at grid points on Γ_P for different values of S , ranging from 0.1 to 2; the grid points now are independent of S . Considering the numerical solution u^{tot} for $S = 2$ as a reference solution, we compute relative errors for different values of S . Numerical results are shown in Figure 14 (b). Clearly, we observe that numerical error decays exponentially at the beginning when S is not very large, and then decays

algebraically for larger S as N is fixed.

Finally, combining Figures 14(a) and 14(b), we see that our numerical solution for the cylindrical wave attains seven significant digits when $N = 2400$ and $S = 1$.

7 Conclusion

For 2D scattering problems in layered media with unbounded interfaces, we developed a PML-based BIE method that relies on the Green's function of PML-transformed free space. The method avoid the difficulty of evaluating the expensive Sommerfeld integrals in common BIE methods based on Green's functions of layered media. Similar to other BIE methods based on the free space Green's function, integral equations are formulated on unbounded interfaces of the background media and these interfaces must be truncated. Although existing methods such as the windowing function method [4, 21, 5, 14], are also effective in truncating interfaces, our method is particularly simple, since the truncation simply follows the well-established PML technique. Notice that the Green's function of PML-transformed free space is simply obtained from the usual Green's function by extending the argument to complex space, and it is very easy to evaluate.

Since our main purpose is to develop a PML-based method and demonstrate its effectiveness for truncating the unbounded interfaces, we have used a simple BIE formulation involving the single- and double-layer boundary integral operators only. In addition, we used the DtN maps to simplify the final linear system. Numerical examples are presented for scattering problems involving two homogeneous media separated by an interface with local perturbations, and possibly with additional obstacles. The integral equations are discretized using a graded mesh technique, Alpert's sixth order hybrid Gauss-trapezoidal rule for logarithmic singularities, and a stabilizing technique. Numerical results indicate that the truncation of interfaces by PML is highly effective, and accurate solutions can be obtained using PMLs with a thickness of one wavelength.

Although our current implementation is somewhat limited, the PML-based BIE method can be extended in a number of directions. Obviously, the method can be used to study scattering problems in multi-layered media with local perturbations, embedded obstacles and penetrable structures. Besides scattering problems, the method can also be used to study eigenvalue problems, such as the problem for guided modes in open waveguide structures. We are planning to address some of these problems in our future works.

Acknowledgement

Y. Y. Lu is partially supported by the Research Grants Council of Hong Kong Special Administrative Region, China (Grant No. CityU 11301914). J. Qian is partially supported by NSF grants 1522249 and 1614566.

Appendix

In this appendix, we will show that equation (41) holds for any $x^o = [x_1^o, x_2^o]$ on Γ_{AB} .

At first, using the Green's representation theorem, we easily see that

$$\tilde{\mathcal{K}}_0[1](x^o) = \lim_{\varepsilon \rightarrow 0^+} 2 \int_{\partial B(x^o, \varepsilon) \cap \bar{\Omega}} \partial_{\nu_c} G_0(x^o, x) 1 ds(x), \quad (83)$$

where $\partial B(x^o, \varepsilon)$ is the boundary of circle $B(x^o, \varepsilon)$ of radius ε centered at x^o , and the unit normal vector ν now points toward Ω .

Thus for sufficiently small ε , one can parameterize $\partial B(x^o, \varepsilon) \cap \bar{\Omega}$ by $x = x^o + \varepsilon(\cos t, \sin t)$ for $t \in [\theta_1, \theta_2]$ where the inner angle $\theta = \theta_2 - \theta_1$.

Clearly, according to its definition (39), we can discretize $\tilde{\mathcal{K}}_0$ as

$$\tilde{\mathcal{K}}_0[1](x^o) = -\frac{1}{\pi} \lim_{\varepsilon \rightarrow 0^+} \int_{\theta_1}^{\theta_2} \frac{(\tilde{x}_1 - \tilde{x}_1^o)\tilde{x}'_2 - \tilde{x}'_1(\tilde{x}_2 - \tilde{x}_2^o)}{|\tilde{x}^o - \tilde{x}|^2} dt. \quad (84)$$

By definitions of complex stretched coordinates transformation (22), on the boundary $\partial B(x^o, \varepsilon) \cap \bar{\Omega}$, we have

$$\begin{aligned} \tilde{x}_1 - \tilde{x}_1^o &= \int_{x_1^o}^{x_1} \alpha_1(s) ds \\ &= \int_{x_1^o}^{x_1^o + \varepsilon \cos t} \alpha_1(s) ds \\ &= \alpha_1(x_1^o) \varepsilon \cos t + O(\varepsilon^2), \end{aligned} \quad (85)$$

and similarly,

$$\tilde{x}_2 - \tilde{x}_2^o = \alpha_2(x_2^o) \varepsilon \sin t + O(\varepsilon^2). \quad (86)$$

Thus,

$$\tilde{\mathcal{K}}_0[1](x^o) = -\frac{1}{\pi} \lim_{\varepsilon \rightarrow 0^+} \int_{\theta_1}^{\theta_2} \frac{\alpha_1(x_1^o) \alpha_2(x_2^o) \varepsilon^2 + O(\varepsilon^3)}{\alpha_1^2(x_1^o) \varepsilon^2 \cos^2 t + \alpha_2^2(x_2^o) \varepsilon^2 \sin^2 t + O(\varepsilon^3)} dt$$

$$= -\frac{1}{\pi} \int_{\theta_1}^{\theta_2} \frac{\alpha_1(x_1^o)\alpha_2(x_2^o)}{\alpha_1^2(x_1^o)\cos^2 t + \alpha_2^2(x_2^o)\sin^2 t} dt. \quad (87)$$

Clearly, if x^o is outside the PML so that $\alpha_1(x^o) = \alpha_2(x^o) = 1$, then

$$\tilde{\mathcal{K}}_0[1](x^o) = -\frac{\theta_2 - \theta_1}{\pi} = -\frac{\theta}{\pi}.$$

If x^o is inside the PML so that x^o is just a smooth point away from the perturbation curve P , then we easily see that $\theta_1 = 0$, $\theta_2 = \pi$, and the inner angle $\theta = \pi$. In this case,

$$\begin{aligned} \tilde{\mathcal{K}}_0[1](x^o) &= -\frac{1}{\pi} \int_0^\pi \frac{\alpha_2(x_2^o)/\alpha_1(x_1^o) \sec^2 t}{(\alpha_2(x_2^o)/\alpha_1(x_1^o) \tan t)^2 + 1} dt \\ &= -\frac{1}{\pi} \left(\int_0^{\pi/2} d(\arctan(\alpha_2/\alpha_1 \tan t)) + \int_{\pi/2}^\pi d(\arctan(\alpha_2/\alpha_1 \tan t)) \right) \\ &= -\frac{1}{\pi} \left(\frac{\pi}{2} - 0 \right) - \frac{1}{\pi} \left(0 - \left(-\frac{\pi}{2}\right) \right) = -\frac{\pi}{\pi}. \end{aligned} \quad (88)$$

References

- [1] B. K. Alpert. Hybrid gauss-trapezoidal quadrature rules. *SIAM Journal on Scientific Computing*, 20(5):1551–1584, 1999.
- [2] J.-P. Berenger. A perfectly matched layer for the absorption of electromagnetic waves. *Journal of Computational Physics*, 114(2):185 – 200, 1994.
- [3] J.-P. Berenger. Three-dimensional perfectly matched layer for the absorption of electromagnetic waves. *Journal of Computational Physics*, 127(2):363 – 379, 1996.
- [4] O. P. Bruno and B. Delourme. Rapidly convergent two-dimensional quasi-periodic Green function throughout the spectrum including wood anomalies. *Journal of Computational Physics*, 262:262 – 290, 2014.
- [5] O. P. Bruno, M. Lyon, C. Pérez-Arancibia, and C. Turc. Windowed green function method for layered-media scattering. *SIAM Journal on Applied Mathematics*, 76(5):1871–1898, 2016.
- [6] W. Cai. Algorithmic issues for electromagnetic scattering in layered media: Green’s functions, current basis, and fast solver. *Advances in Computational Mathematics*, 16(2):157–174, 2002.

- [7] W. Cai. *Computational Methods for Electromagnetic Phenomena*. Cambridge University Press, New York, NY, 2013.
- [8] W. Cai and T. J. Yu. Fast calculations of dyadic Green’s functions for Electromagnetic scattering in a multilayered medium. *J. Comput. Phys.*, 5(5):247–251, 2000.
- [9] Z. Chen and X. Xiang. A source transfer domain decomposition method for Helmholtz equations in unbounded domain. *SIAM Journal on Numerical Analysis*, 51(4):2331–2356, 2013.
- [10] W. C. Chew. *Waves and fields in inhomogeneous media*. IEEE PRESS, New York, 1995.
- [11] D. Colton and R. Kress. *Inverse Acoustic and Electromagnetic Scattering Theory (3rd Edition)*. Springer, 2013.
- [12] T.J. Cui and W.C. Chew. Efficient evaluation of Sommerfeld integrals for tm wave scattering by buried objects. *Journal of Electromagnetic Waves and Applications*, 12(5):607–657, 1998.
- [13] T.J. Cui and W.C. Chew. Fast evaluation of Sommerfeld integrals for em scattering and radiation by three-dimensional buried objects. *IEEE Transactions on Geoscience and Remote Sensing*, 37(2):887–900, Mar 1999.
- [14] J. Lai, L. Greengard, and M. O’Neil. A new hybrid integral representation for frequency domain scattering in layered media. *submitted*, arXiv:1507.04445v2, 2015.
- [15] Matti Lassas and Erkki Somersalo. Analysis of the PML equations in general convex geometry. *Proceedings of the Royal Society of Edinburgh: Section A Mathematics*, 131(5):1183–1207, 2001.
- [16] W. Lu and Y. Y. Lu. Efficient high order waveguide mode solvers based on boundary integral equations. *Journal of Computational Physics*, 272:507 – 525, 2014.
- [17] W. McLean. *Strongly Elliptic Systems and Boundary Integral Equations*. Cambridge University Press, 2000.
- [18] A. Meier and S. N. Chandler-Wilde. On the stability and convergence of the finite section method for integral equation formulations of rough surface scattering. *Mathematical Methods in the Applied Sciences*, 24(4):209–232, 2001.

- [19] D. Miret, G. Soriano, and M. Saillard. Rigorous simulations of microwave scattering from finite conductivity two-dimensional sea surfaces at low grazing angles. *IEEE Transactions on Geoscience and Remote Sensing*, 52(6):3150–3158, June 2014.
- [20] P. Monk. *Finite Element Methods for Maxwell's Equations*. Oxford University Press, 2003.
- [21] J. A. Monro. *A super-algebraically convergent, windowing-based approach to the evaluation of scattering from periodic rough surfaces*. Dissertation (Ph.D.), California Institute of Technology., 2008.
- [22] M. Ochmann. The complex equivalent source method for sound propagation over an impedance plane. *The Journal of the Acoustical Society of America*, 116(6), 2004.
- [23] V. I. Okhmatovski and A. C. Cangellaris. Evaluation of layered media Green's functions via rational function fitting. *IEEE Microwave and Wireless Components Letters*, 14(1):22–24, Jan 2004.
- [24] M. Paulus, P. Gay-Balmaz, and O. J. F. Martin. Accurate and efficient computation of the Green's tensor for stratified media. *Phys. Rev. E*, 62:5797–5807, Oct 2000.
- [25] C. Pérez-Arancibia and O. P. Bruno. High-order integral equation methods for problems of scattering by bumps and cavities on half-planes. *J. Opt. Soc. Am. A*, 31(8):1738–1746, Aug 2014.
- [26] Balth Van Der Pol. Theory of the reflection of the light from a point source by a finitely conducting flat mirror, with an application to radiotelegraphy. *Physica*, 2(1):843 – 853, 1935.
- [27] M. Saillard and G. Soriano. Rough surface scattering at low-grazing incidence: A dedicated model. *Radio Science*, 46(5):n/a–n/a, 2011. RS0E13.
- [28] A. Sommerfeld. Über die ausbreitung der wellen in der drahtlosen telegraphie. *Annalen der Physik*, 333(4):665–736, 1909.
- [29] P. Spiga, G. Soriano, and M. Saillard. Scattering of electromagnetic waves from rough surfaces: A boundary integral method for low-grazing angles. *IEEE Transactions on Antennas and Propagation*, 56(7):2043–2050, July 2008.

- [30] G. Taraldsen. The complex image method. *Wave Motion*, 43(1):91 – 97, 2005.
- [31] D. J. Thomson and J. T. Weaver. The complex image approximation for induction in a multilayered earth. *Journal of Geophysical Research*, 80(1):123–129, 1975.
- [32] L. N. Trefethen. *Spectral Methods in MATLAB*. SIAM, 2000.
- [33] H. Weyl. Ausbreitung elektromagnetischer wellen über einem ebenen leiter. *Annalen der Physik*, 365(21):481–500, 1919.
- [34] Z. Zhao, L. Li, J. Smith, and L. Carin. Analysis of scattering from very large three-dimensional rough surfaces using mlfmm and ray-based analyses. *IEEE Antennas and Propagation Magazine*, 47(3):20–30, June 2005.